Eur. Phys. J. D (2023)77:45
https://doi.org/10.1140/epjd/s10053-023-00622-8

THE EUROPEAN PHYSICAL JOURNAL D

Regular Article – Atomic and Molecular Collisions

Collisional excitation and photoexcitation of Ca IV including a strong 3.2 μm emission line

Sultana N. Nahar[1,a] and Bilal Shafique[2,b]

[1] Astronomy Department, The Ohio State University, 140 W. 18th Ave, Columbus, OH 43210, USA
[2] Physics Department, University of Azad Jammu and Kashmir, Muzzafarabad 13100, Kashmir, Pakistan

Received 22 October 2022 / Accepted 20 February 2023

Abstract. We report a detailed study of features of electron impact excitation (EIE) of Ca IV (Ca IV + e → Ca IV* + e' → Ca IV + h$\nu + e'$), for the first time using the relativistic Breit–Pauli R-matrix method with a large close-coupling wave function expansion of 54 fine structure levels belonging to $n = 2, 3, 4$ complexes. Calcium lines in the infrared (IR) region are expected to be observed by the high-resolution James Webb Space Telescope. Our study predicts the presence of a strong 3.2 μm emission line in IR formed due to EIE of $3p^5\ ^2P^o_{3/2} - 3p^5\ ^2P^o_{1/2}$ in Ca IV. The EIE collision strength (Ω) for the transition shows extensive resonance with enhanced background (top panel, Figure below), resulting in an effective collision strength (Υ) of 2.2 at about 10^4 K that increases to 9.66 around 3×10^5 k (lower panel, Figure below). The present results include Ω for all 1431 excitations among the 54 levels and Υ for a limited number of transitions of possible interest. We found extensive resonances in the low-energy region of Ω, and convergence of the resonances and of the partial waves with the 54-level wave function. At high energy, Ω decreases beyond the resonance region for forbidden transitions and is almost constant or decreases slowly for dipole-allowed transitions with low oscillation strength (f-values) and increases with Coulomb–Bethe behavior of ln(E) to almost a plateau for transitions with high f-values. The wave function of Ca IV was obtained from optimization of 13 configurations $3s^23p^5, 3s3p^6, 3s^23p^43d, 3s^23p^44s, 3s^23p^44p, 3s^23p^44d, 3s^23p^44f, 3s^23p^45s, 3s3p^53d, 3s3p^54s, 3s3p^54p, 3p^63d, 3s3p^43d^2$, each with the core configuration of $1s^22s^22p^6$, using the SUPERSTRUCTURE atomic structure program. They produce 387 fine structure levels. We report transition parameters—oscillator strength, line strength (S) and A-values-for a total of 93,296 electric dipole (E1), quadrupole (E2), octupole (E3), magnetic dipole (M1) and quadrupole (M2) transitions among these levels. The lifetimes of these levels are also presented.

1 Introduction

Calcium is one of most abundant biogenic elements which is created during supernova (SN) explosions. Lines of Ca I and II are seen in cool stars. H and K lines and forbidden lines of Ca II are commonly detected in supernovae (e.g., [1]). The lines can determine the abundance of the element in the object. Asplund et al. [2] obtained Ca abundance in the sun with respect to hydrogen, in logarithmic abundances, to be log[e(Ca)] = 6.34 ± 0.04 where log[e(Ca)] = 12 + log[N(Ca)/N(H)], H is defined as logH = 12.00, and N(Ca) and N(H) are the number densities of elements Ca and H, respectively. Much attention has recently been focused on Ca-rich supernovae, such as SN 2019ehk in the star-forming spiral galaxy Messier 100, about 55 million light years from the earth, first reported by Shepherd [3] and analyzed by Jacobson-Galan et al. [4]. Jacobson-Galan et al.[4] found that the calcium-rich SN belongs to the calcium-strong transient (CaST) class. Ca-IV lines in the infrared (IR) region were observed in the NGC 7027 nebula by Feuchtgruber et al. [5]. The 3.2 μm line was observed in three Wolf–Rayet stars and was used to determine abundance and wind speed by Ignance et al. [6]. Furthermore, emission lines of two calcium ions, Ca-V and Ca-VII, were observed in the NGC 2707 and NGC 6302 nebulae [7], and Ca II lines were observed in the high-temperature environment of white dwarfs [8].

The present work reports the study of two atomic processes of Ca IV that produce spectral lines, electron impact excitation (EIE) and photoexcitation. EIE is one of the most common atomic processes in near empty space or in astrophysical plasmas with or without a radiative source. A traveling electron interacts with an ion and transfers part of its energy to promote the ion

Sultana Nahar and Bilal Shafique have contributed equally to this work

[a] e-mail: nahar.1@osu.edu (corresponding author)
[b] e-mail: bilalshafiquekhawaja@ajku.edu.pk

Published online: 20 March 2023

to an excited state. This is followed by de-excitation of the target ion by emission of a photon (e.g., [9])

$$X^{+z} + e \rightarrow X^{+z*} + e' \rightarrow X^{+z} + h\nu + e' \qquad (1)$$

where X^{+z} is the target ion of charge z. The emitted photon can form an observable line depending on the radiative transfer and density of the plasma. The projectile electron can also form a quasi-bound state by exciting the target ion to a higher energy state, E^{**}, while attaching itself to an orbit νl, which happens very commonly in nature, matching the energy of a doubly excited autoionizing Rydberg state

$$E_x \nu l = E^{**}(X^{+z}\nu l) = E_x - z^2/\nu^2 \qquad (2)$$

before going out free. This intermediate state introduces a resonance in the collisional scattering. E_x is the excited energy of the ion, and νl are the effective quantum number and angular momentum of the scattered electron with respect of E_x. The present study implements close-coupling (CC) wave function expansion that produces the autoionizing resonances automatically.

The other process, photoexcitation/de-excitation, forms a line as the ion absorbs or emits a photon

$$X^{+z} + h\nu \leftrightarrow X^{+z*} \qquad (3)$$

This process occurs most commonly when there is a radiative source, such as a star shining due to the plasma state of matter.

Among the low ionization stages of Ca, Ca IV has been the least studied ion. No study on its EIE is found in the literature. EIE of Ca IV is the main focus of the present study.

Among the past studies on energies and transitions, Sugar and Corliss [10] compiled the experimentally measured energy levels of Ca IV which are available at the National Institute of Standards and Technology (NIST) website [11] (www.nist.gov). The radiative transition rates of Ca IV were reported by Naqvi [12], Varsavsky [13], Fawcett and Gabriel [14], Huang et al. [15], Wilson et al. [16] and Gabriel et al. [17], who identified several lines generated from observed UV transitions. The probability of detection of Ca IV lines has increased considerably with the high-resolution observation of the James Webb Space Telescope (JWST) in the IR region. The present work reports collisional excitation and photoexcitation for many levels of Ca IV which include collision strength (Ω) and the Maxwellian averaged collision strength or effective collision strength (Υ), and parameters f-, $S-$ and $A-$ values for radiative transitions.

2 Theoretical approximation

We present a brief outline of the theoretical background for EIE and radiative photoexcitation below as guidance for the reader. More details can be found, for example, in Pradhan and Nahar [9]. We have treated EIE of Ca IV for collision strength with the relativistic Breit–Pauli R-matrix (BPRM) method, as developed under the Iron Project (IP, [18,19]). We used a wave function expansion in the CC approximation that includes excitation to $n = 2, 3, 4$ levels in the target and obtained collision strength. We obtained radiative transition parameters for an extensive set of transitions using relativistic Breit–Pauli approximation implemented in the atomic structure program SUPERSTRUCTURE (SS, [20,21]).

Although two approaches are used for collision and photoexcitation, the computations are related. BPRM calculations are initiated with the wave function expansion of the target ion, such as Ca IV, generated by the SS program. We first discuss the outlines of collisional excitation, and then photoexcitation or radiative transitions.

2.1 Breit–Pauli R-matrix (BPRM) calculations for EIE

The BPRM Hamiltonian as adopted under the IP [18, 19] in atomic Rydberg units is given by

$$H^{\rm BP}_{N+1} = \sum_{i=1}^{N+1}\left\{-\nabla_i^2 - \frac{2Z}{r_i}\right\} + \sum_{j>i}^{N+1}\frac{2}{r_{ij}} + H^{\rm mass}_{N+1} + H^{\rm Dar}_{N+1} + H^{\rm so}_{N+1}. \qquad (4)$$

where the first three terms belong to the non-relativistic Hamiltonian and the last three terms are the one-body relativistic corrections which are mass, Darwin, and spin–orbit interaction terms, respectively. BPRM codes include all of these terms and some of the two-body correction terms of the Breit-interaction (e.g. [9]). One Rydberg (Ry) is half of a Hartree giving the factor 2 in the terms.

BPRM calculations start with the target ion wave function generated by SS and calculate the wave function of the total atomic system of the target ion and the interacting electron in the CC approximation. In the CC approximation, the wave function of (e+ion) in a state $SL\pi J$, where S is total spin, L is the orbital, and J is the total angular momenta, is expressed as

$$\Psi_E(e + ion) = A\sum_i^n \chi_i(ion)\theta_i + \sum_j c_j\Phi_j(e + ion) \qquad (5)$$

In the first term, $\chi_i(ion)$ is the wave function expansion of the target ion, and θ_i is that of the interacting electron, in channel $S_tL_t\pi_tJ_tk_i^2l(SL\pi J)$, where $S_tL_t\pi_tJ_t$ is the target ion state interacting with the projectile electron of energy k_i^2 and orbital angular momentum l. The sum represents the ground state and various excited states of the target ion. A is the anti-symmetrization operator. In the second term, $\Phi_j(e+ion)$ represents the

(target + electron) wave function, basically part of the first term separated out to show the orthogonality condition of the interacting electron and short-range interaction. CC wave function expansion, which includes target ion excitations, enables resonances to be produced inherently. The interference of the bound states of the target ion and the projectile electron continuum wave function in the transition matrix introduces the resonances. Substitution of the CC expansion in the Schrodinger equation with the Breit–Pauli Hamiltonian results in a set of coupled equations. The R-matrix method is used to solve this set of equations for the energy and wave functions of the (e+ion) system.

The scattering matrix for the transition of the target ion from state i to state k by collision, $\mathbf{S}_{SL\pi J}(S_iL_iJ_il - S_kL_kJ_kl')$, where $SL\pi J$ is the (e+ion) state, and l and l' are the incident and scattered partial waves of the free electron, is derived from the reactant matrix of the incident wave (e.g., [9,22–24]). The collision strength Ω for EIE is given by

$$\Omega(S_iL_iJ_i - S_kL_kJ_k) = \frac{1}{2}\sum_{SL\pi J}\sum_{l,l'}(2J+1)|r\mathbf{S}_{SL\pi J}(S_iL_iJ_il - S_kL_kJ_kl')|^2 \quad (6)$$

Ω reveals the detailed features with resonances of the collision. The plasma models use the temperature-dependent quantity, the effective collision strength $\Upsilon(T)$, which is obtained by averaging Ω over the Maxwellian distribution function of the electrons at temperature T_e as

$$\Upsilon_{ij}(T_e) = \int_0^\infty \Omega_{ij}(E)\exp(-E/kT_e)d(E/kT_e), \quad (7)$$

where k is the Boltzmann constant and E is the energy of the projectile electron after the excitation, that is, the energy of the scattered electron. The excitation rate coefficient $(q_{ij}(T_e))$ is related to the effective collision strength Υ_{ij} as

$$q_{ij}(T_e) = \frac{8.63\times10^{-6}}{g_iT_e^{1/2}}e^{-E_{ij}/kT_e}\Upsilon_{ij}(T_e)cm^3/s, \quad (8)$$

where g_i is the statistical weight of the initial level, T is in K, E_{ij} is the transition energy in Rydberg, and $(1/\mathrm{kT} = 157885/\mathrm{T})$.

The high-energy background of collision strength shows certain general behaviors depending on the type of excitation. The background of Ω is the smooth curve at the base of resonant features. For forbidden transitions, Ω decreases to almost zero with higher energy. For dipole-allowed transitions, using the Born approximation with a coulombic wave function, Ω shows a high-energy limiting behavior and is given by the Coulomb–Bethe approximation

$$\Omega_{ij}(E) = \frac{4g_if_{ij}}{E_{ij}}ln\frac{E}{E_{ij}}, \quad (9)$$

where f_{ij} is the oscillator strength for a dipole-allowed transition, and E is the incident electron energy. In the high-energy limit,

$$\Omega_{ij}(E) \sim_{E\to\infty} d_{ij}ln(E) \quad (10)$$

where d_{ij} is proportional to the oscillator strength. The logarithmic function will increase with an increase in electron energy, but the rising trend of the function slows with very high values of the argument. Hence, for a low value of d, Ω may not change, as it is multiplied by a small number. For high values of d, Ω will increase but will lead to a plateau.

2.2 Atomic structure calculations for radiative transitions

Theoretical details for obtaining radiative transition parameters through atomic structure calculations using the SUPERSTRUCTURE (SS) program can be found, for example, in [9,21]. The Hamiltonian includes relativistic mass, Darwin, and spin–orbit interaction correction terms, full two-body Breit interaction and some additional two-body terms. The interacting electron and core ion potential, implemented in SS, is represented by the Thomas–Fermi–Amaldi–Dirac potential. The program uses configuration interaction wave function expansion, which for a symmetry $J\pi$ can be expressed as

$$\Psi(J\pi) = \sum_{i=1}^{N} a_i\psi[C_i(J\pi)] \quad (11)$$

where a_is is the amplitude or the mixing coefficient of the wave function of configuration $C_i, \psi[C_i(\mathrm{J}\pi)]$ with symmetry $J\pi$, and the sum is over all N configurations that can produce a level of symmetry $J\pi$. The wave function results in N eigenvalues from the Hamiltonian matrix, and each eigenvalue corresponds to an energy of one level of symmetry. The accuracy of the energy of a level may depend on the size of the expansion and the value of the mixing coefficient (e.g., [9].)

The transition matrix element, for example, for electric dipole allowed transition (E1), is given by $< \Psi_B||\mathbf{D}||\Psi_{B'} >$, where Ψ_B and $\Psi_{B'}$ are the initial and final state bound wave functions, and $\mathbf{D} = \sum_i \mathbf{r}_i$ is the dipole operator where the sum is over the number of electrons. The line strength $\mathbf{S}$ is obtained from the modulus squared of the transition matrix,

$$S = |\left\langle \Psi_f|\sum_{j=1}^{N+1} r_j|\Psi_i\right\rangle|^2 \quad (12)$$

where Ψ_i and Ψ_f are the initial and final wave functions. The transition parameters, oscillator strength (f_{ij}) and radiative decay rate (A) can be obtained from

line strength as

$$f_{ij} = \frac{E_{ji}}{3g_i}\mathbf{S}, \quad A_{ji}(sec^{-1}) = \left[0.8032 \times 10^{10}\frac{E_{ji}^3}{3g_j}\right]\mathbf{S} \tag{13}$$

The transition probabilities for the electric quadrupole (E2), magnetic dipole (M1), electric octupole (E3) and magnetic quadrupole (M2) transition parameters can be obtained from their respective line strengths (e.g., [9,21]).

The lifetime of an excited level can be obtained from the inverse of the sum of all transition probabilities to lower levels,

$$\tau_i(s) = 1/\left[\sum_j A_{ji}(s^{-1})\right] \tag{14}$$

In atomic units of time $\tau_0 = 2.4191 \times 10^{-17}$s, the transition probabilities or the radiative decay rate can be expressed as $A_{ji}(s^{-1}) = A_{ji}(a.u.)/\tau_0$.

3 Computation

The R-matrix calculations start with the target wave functions as an input. These wave functions are obtained from atomic structure calculations, mainly using SS [20,21]. The Ca-IV wave function, energies and the relevant radiative transition parameters were obtained from an optimized set of 13 configurations of the ion, $3s^23p^5$, $3s3p^6$, $3s^23p^43d$, $3s^23p^44s$, $3s^23p^44p$, $3s^23p^44d$, $3s^23p^44f$, $3s^23p^45s$, $3s3p^53d$, $3s3p^54s$, $3s3p^54p$, $3p^63d$ and $3s3p^43d^2$, with the same core configuration $1s^22s^22p^6$ for each, using SS. The set of optimized Thomas–Fermi orbital scaling parameters are 1.268 65(1 s), 1.0395(2 s), 1.04288(2p), 1.1(3 s), 1.1(3p), 1.1(3d), 1.083(4 s), 1.079(4p), 1.031(4d), 1.1 (4f) and 1.1 (5 s), respectively. The configuration set provided 387 fine structure levels, 54 of which were considered for the collisional excitation in the present study and hence were used in the wave function expansion of Ca IV. Selecting a set of levels of the target or core ion from a large set is the standard for an R-matrix calculation. The computation of collision strength, which depends on the size of the wave function expansion, required several hundreds of CPU hours on the high-performance computers at the Ohio Supercomputer Center.

The purpose of an optimized set of configurations, which produce a large set of levels, is to ensure that contributions from configuration interactions are included in the wave functions of levels, and thus can provide a set of levels, starting from the ground level, of higher accuracy for the CC wave function expansion. The inclusion of all levels, 387 in the present case, in the calculations will require considerable computational time, and is likely to be computationally prohibitive, which is very common and hence impractical to consider. The set of excited levels considered for an R-matrix calculation is typically based on the expected physics to be revealed, mainly the resonant features. No new physics was expected from levels higher than 54, since the resonances would have converged, and hence those belonging to higher levels would no longer be strong but would have weakened to converge to the background. This was also our finding, as demonstrated in the Results section.

Table 1 presents the 54 fine structure levels of Ca IV included in the wave function expansion and compares the calculated energies from SS with experimental values tabulated by NIST. The comparison shows that the present computed energies are generally within a few percent of the observed values. The accuracy of a level energy depends on how well the wave function expansion represents the level through interaction of the given set of configurations. For more precise energy positions of the resonances in EIE collision strength, we have replaced the calculated energies with the available observed energies in the BPRM calculations.

It is important to ensure convergence in contributions by the number of partial waves and (e+ion) symmetries to the collision strengths Ω. We computed Ω several times by varying the sets of partial waves l up to 22 and (e-ion) symmetries J up to ≤ 22 of even and odd parities. We found that (i) the Ω background is converged with the highest values of $l = 20$ and $J\pi = 11$, and (ii) the larger number of l and $J\pi$ than these introduced computational instability which gives NaN (Not a Number) for the collision strengths at various electron energies.

Obtaining "NaN" for Ω values is a known problem for an R-matrix calculation. These values are introduced when the computation goes through very small numbers. Usually, the NaN points are deleted from the sets of Ω values. However, we made attempts to get approximate values of Ω at energies of NaN values obtained with large l and J values by extrapolating or interpolating the neighboring Ω points. Smooth background can be extrapolated but resonances are not reproduced in Ω as can be seen in the blue (with extrapolation) and red curves (no extrapolation) in Fig. 1 representing the same excitation of the ion. The resonant peaks of the blue curve, which has many NaN points and interpolation was carried out to replace the NaNs with real numbers, are lower than the red curves.

Figure 1 also demonstrates the test of convergence of Ω for a few sets of the highest values of l and J for the excitations of (a) $^2P^o_{3/2} - ^2P^o_{1/2}$ and (b) $^2P^o_{1/2} - ^2S_{1/2}$ computed at a coarse energy mesh. The red curves correspond to the use of $l = 0$–20 and $J\pi = 0$–11, the blue curves to $l = 0$–22 and $J\pi = 0$–21, and the magenta curves to $l = 0$–11 and $J\pi = 0$–10. The magenta curves of Ω ($l = 0$–11 and $J\pi = 0$–10) are considerably lower than the other curves, indicating that convergence of contributions from 12 partial waves has not been reached. The blue and red curves have about the same background, indicating that convergence in contributions of partial waves has been reached. Hence,

Table 1 Comparison of the present calculated energies for the 54 fine structure levels of Ca IV with those available (Sugar and Corliss [10]) in the compilation table of NIST [11]

K	Configuration	Term	$E_{present}$ (Ry)	E_{NIST} (Ry)	% diff
1	$3s^2 3p^5$	$^2P^o_{3/2}$	0	0	0.0
2	$3s^2 3p^5$	$^2P^o_{1/2}$	0.0302	0.0284	5.9
3	$3s3p^6$	$^2S_{1/2}$	1.3031	1.3891	6.2
4	$3s^2 3p^4 3d$	$^4D_{7/2}$	1.8197	1.8362	0.9
5	$3s^2 3p^4 3d$	$^4D_{5/2}$	1.8218	1.8385	0.9
6	$3s^2 3p^4 3d$	$^4D_{3/2}$	1.8243	1.8410	0.9
7	$3s^2 3p^4 3d$	$^4D_{1/2}$	1.8263	1.8431	0.9
8	$3s^2 3p^4 3d$	$^4F_{9/2}$	1.9901	1.9865	0.2
9	$3s^2 3p^4 3d$	$^4F_{7/2}$	1.9999	1.9964	0.2
10	$3s^2 3p^4 3d$	$^2P_{3/2}$	2.0047.	1.9965	0.4
11	$3s^2 3p^4 3d$	$^2P_{1/2}$	2.0070	2.0036	0.2
12	$3s^2 3p^4 3d$	$^4F_{5/2}$	2.0115	2.0083	0.2
13	$3s^2 3p^4 3d$	$^4F_{3/2}$	2.0225.	2.0149	0.4
14	$3s^2 3p^4 3d$	$^4P_{5/2}$	2.0705.	2.0473	0.2
15	$3s^2 3p^4 3d$	$^4P_{3/2}$	2.0761	2.0536	1.1
16	$3s^2 3p^4 3d$	$^2D_{3/2}$	2.0817	2.0732	0.4
17	$3s^2 3p^4 3d$	$^4P_{1/2}$	2.0840	2.0616	1.0
18	$3s^2 3p^4 3d$	$^2D_{5/2}$	2.0970	2.0890	0.4
19	$3s^2 3p^4 3d$	$^2F_{7/2}$	2.1076	2.1074	0.02
20	$3s^2 3p^4 3d$	$^2F_{5/2}$	2.1310	2.1297	0.06
21	$3s^2 3p^4 3d$	$^2G_{7/2}$	2.1369	2.1573	0.95
22	$3s^2 3p^4 3d$	$^2G_{9/2}$	2.1382	2.1571	0.88
23	$3s^2 3p^4 3d$	$^2F_{7/2}$	2.2990	2.3051	0.26
24	$3s^2 3p^4 3d$	$^2F_{5/2}$	2.3046	2.3109	0.27
25	$3s^2 3p^4 3d$	$^2D_{5/2}$	2.4602	2.4937	1.36
26	$3s^2 3p^4 3d$	$^2D_{3/2}$	2.4653	2.4993	1.34
27	$3s^2 3p^4 3d$	$^2S_{1/2}$	2.6559	2.6979	1.8
28	$3s^2 3p^4 4s$	$^4P_{5/2}$	2.6688	2.7714	3.7
29	$3s^2 3p^4 4s$	$^4P_{1/2}$	2.6701	2.7972	4.5
30	$3s^2 3p^4 4s$	$^2P_{3/2}$	2.6780	2.7974	4.24
31	$3s^2 3p^4 4s$	$^4P_{3/2}$	2.6818	2.7857	3.6
32	$3s^2 3p^4 4s$	$^2P_{1/2}$	2.6895	2.8098	4.3
33	$3s^2 3p^4 3d$	$^2D_{5/2}$	2.7449	2.8566	4.2
34	$3s^2 3p^4 3d$	$^2P_{3/2}$	2.7495	2.8976	5.2
35	$3s^2 3p^4 3d$	$^2P_{1/2}$	2.7666	2.9135	4.9
36	$3s^2 3p^4 4s$	$^2D_{3/2}$	2.7689	2.8794	3.8
37	$3s^2 3p^4 4s$	$^2D_{5/2}$	2.8479	2.9941	4.7
38	$3s^2 3p^4 3d$	$^2D_{3/2}$	2.8491	2.9961	4.7
39	$3s^2 3p^4 4p$	$^4P^o_{5/2}$	3.0145	3.1268	3.8
40	$3s^2 3p^4 4p$	$^4P^o_{3/2}$	3.0179	3.1318	3.5
41	$3s^2 3p^4 4p$	$^4P^o_{1/2}$	3.0251	3.1386	3.5
42	$3s^2 3p^4 4p$	$^4D^o_{7/2}$	3.0539	3.1829	4.1
43	$3s^2 3p^4 4p$	$^4D^o_{5/2}$	3.0610	3.1913	4.0
44	$3s^2 3p^4 4p$	$^4D^o_{3/2}$	3.0706	3.1996	4.0
45	$3s^2 3p^4 4p$	$^2P^o_{1/2}$	3.0729	3.2128	4.3
46	$3s^2 3p^4 4p$	$^4D^o_{1/2}$	3.0751	3.2039	4.0
47	$3s^2 3p^4 4p$	$^2D^o_{5/2}$	3.0824	3.2185	4.0
48	$3s^2 3p^4 4s$	$^2S_{1/2}$	3.0828	3.2573	5.4
49	$3s^2 3p^4 4p$	$^2D^o_{3/2}$	3.0888	3.2376	4.0
50	$3s^2 3p^4 4p$	$^2P^o_{3/2}$	3.1017	3.2209	3.7
51	$3s^2 3p^4 4p$	$^4S^o_{3/2}$	3.1217	3.2577	4.0
52	$3s^2 3p^4 4p$	$^2S^o_{1/2}$	3.1249	3.2598	4.0
53	$3s^2 3p^4 4p$	$^2F^o_{7/2}$	3.2091	3.3629	4.5
54	$3s^2 3p^4 4p$	$^2F^o_{5/2}$	3.2133	3.3591	4.5

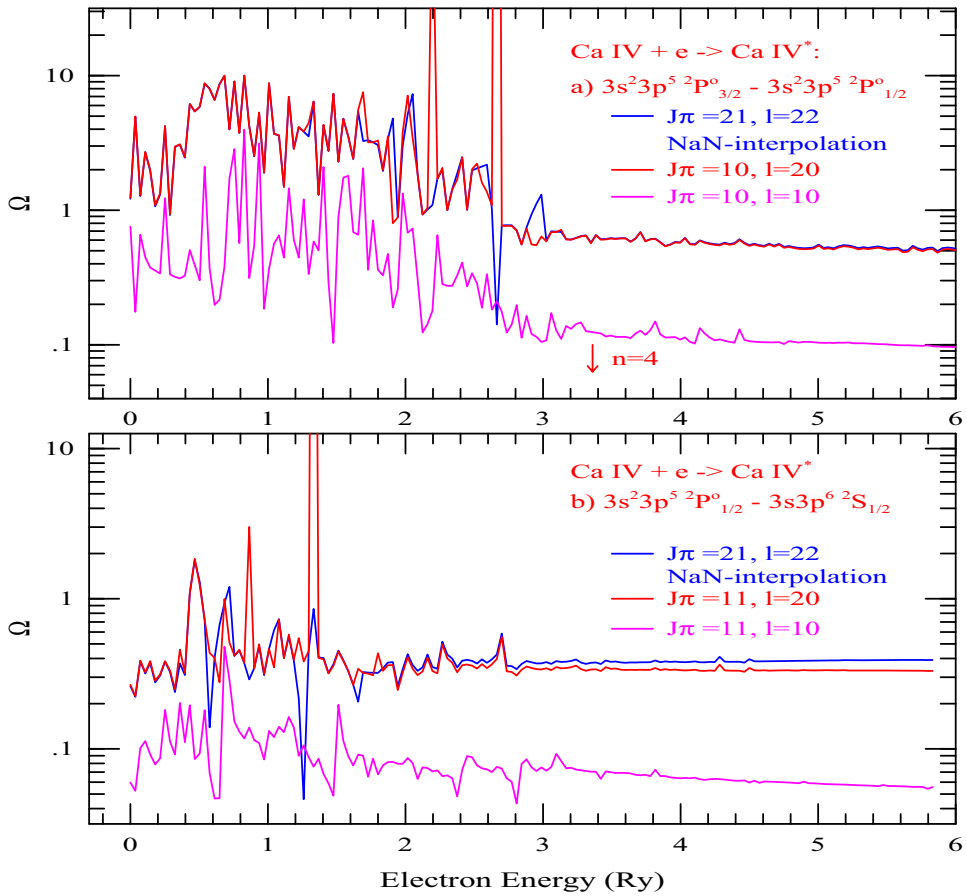

Fig. 1 Demonstration of convergence of contributions of partial waves with various l and J values to Ω. The x-axis corresponds to the energy of the scattered electron after the excitation which starts with zero energy. Red curves indicate the best convergent condition

specifications for the red curve, $l = 0$–20 and $J\pi = 0$–11, have been used for the computation of Ω. Final Ω values were obtained at fine energy meshes. We used a very fine energy mesh of $\Delta E < 10^{-6}$ Ry to resolve the near-threshold resonances.

The above discussion concerns the impact of partial waves that are noticeable. Beyond this, top-up contributions are added. As top-up contributions, we included contributions of higher multipole potentials to Ω using the option ipert = 1 in STGF of the R-matrix codes. The other top-up contributions come from higher partial waves beyond those specified, using the option chosen as ipert = 2, in STGF. The approximation incorporated in the R-matrix code STGF is most likely based on the treatment of Burgess and Tully [25] of higher partial waves. However, computation of contributions of the higher partial waves not only takes much longer, but it is not done for most cases as it stops due to numerical issues except for a few excitations and at some energies. We computed the contributions of higher partial waves when it was possible to test them and found negligible contributions in increasing the Ω values to affect the average collision strengths Υ. The problem is compensated, as done in the present case, by including a larger number of partial waves without the approximation.

The program ecs-omg.f [26] was used to calculate the effective collision strengths Υ, Eq. (7), at various temperatures, where Ω is integrated over the energy of the scattered electron from zero to a high value. The high-energy limit is chosen as a value at which Ω has diminished to a near-zero value or has reached a plateau, and the exponential factor of Υ has approached a near-zero value. Ω points between the highest electron energy computed by the BPRM codes to the highest energy limit of the Υ integral are obtained using the logarithmic behavior of the Coulomb–Bethe approximation in Eq. (10).

The radiative data of $f-$ and $A-$values for dipole-allowed photoexcitation (E1) have been reprocessed with experimental energies using code PRCSS (e.g. [27]). This allows us to obtain the transition parameters at the observed wavelengths. For the reprocessing, the transition energies were obtained from the experimental-level energies and then multiplied, following Eq. 13, to the calculated line strengths from SUPERSTRUCTURE code. For the levels for which no observed or measured values are available, calculated energies were used.

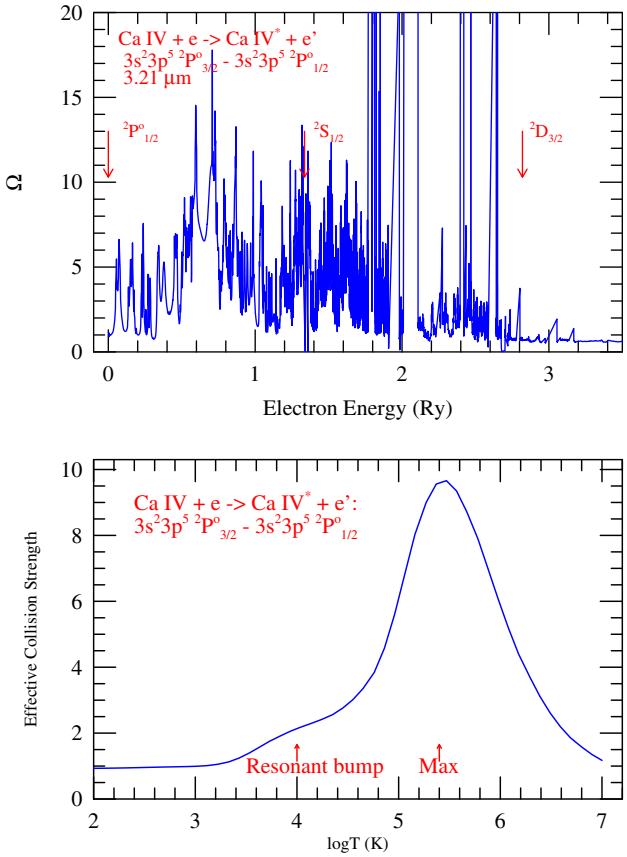

Fig. 2 Upper panel: EIE collision strength (Ω) of Ca IV for the first excitation $3s^2 3p^5\ ^2P^o_{3/2} - 3s^2 3p^5\ ^2P^o_{1/2}$ of the ground level with respect to scattered electron energy in Rydberg units. Extensive resonances with enhanced background can be noted within the energy region of dipole-allowed transitions from the ground level $3s^2 3p^5\ ^2P^o_{3/2}$ up to $^2D^o_{1/2}$. Lower panel: Effective collision strength for $3\,s^2 3p^5\ ^2P^o_{3/2} - 3\,s^2 3p^5\ ^2P^o_{1/2}$ excitation in Ca IV showing a high peak value at about 3×10^5 K, indicating high probability of detection of the line by JWST

4 Results and discussion

We present the atomic parameters for EIE of (e + Ca IV $\rightarrow$ Ca IV* + e' $\rightarrow$ Ca IV + hν + e') and photoexcitation of Ca IV + hν $\leftrightarrow$ Ca IV*. The results for the collisional excitation are reported for the first time, as indicated by a literature search. They are described below, followed by those for photoexcitation.

4.1 Collisional excitation of Ca IV

We discuss the characteristic features of collisional excitation with illustrative examples. The first excitation of the target is usually of particular interest because of its high probability through EIE, and the emitted photon, typically of low energy, can travel for a long time without being absorbed. If the corresponding emission line is strong, it can be easily detected in low-density plasmas and used for identification of the ion and environmental diagnostics. The first excitation in Ca IV, $3p^5\ ^2P^o_{3/2} - 3p^5\ ^2P^o_{1/2}$, within the ground configuration is of particular importance since the wavelength of the emission line, 3.207 μm, is well within the high-resolution IR wavelength detection range, 0.6–28.3 μm, of the JWST and can be used for diagnostics and abundances (e.g., [6]).

The upper panel of Fig. 2 presents collision strength for the first excitation $\Omega(^2P^o_{3/2} -^2 P^o_{1/2})$ of the target Ca-IV ion with respect to scattered electron energy after the excitation. The electron energy is relative to the excitation threshold and hence starts at zero. We note that Ω for the collisional excitation is quite strong as it shows extensive resonances with enhanced background in the energy region between the first excited level, $^2P^o_{1/2}$, and the next one, $^2S_{1/2}$ (indicated by arrows), and continues to be strong beyond it up to the $^2D_{3/2}$ level, the one before the last dipole-allowed transition in the 54-level wave function expansion. Beyond $^2D_{3/2}$, all but one of the transitions are forbidden, and the resonances become weaker. There are 29 dipole-allowed levels in total in this energy range. Each excitation of the target ion corresponds to a Rydberg series of resonances. Typically, the resonances corresponding to a dipole-allowed excitation are visible while others are suppressed. The resonances belonging to very high

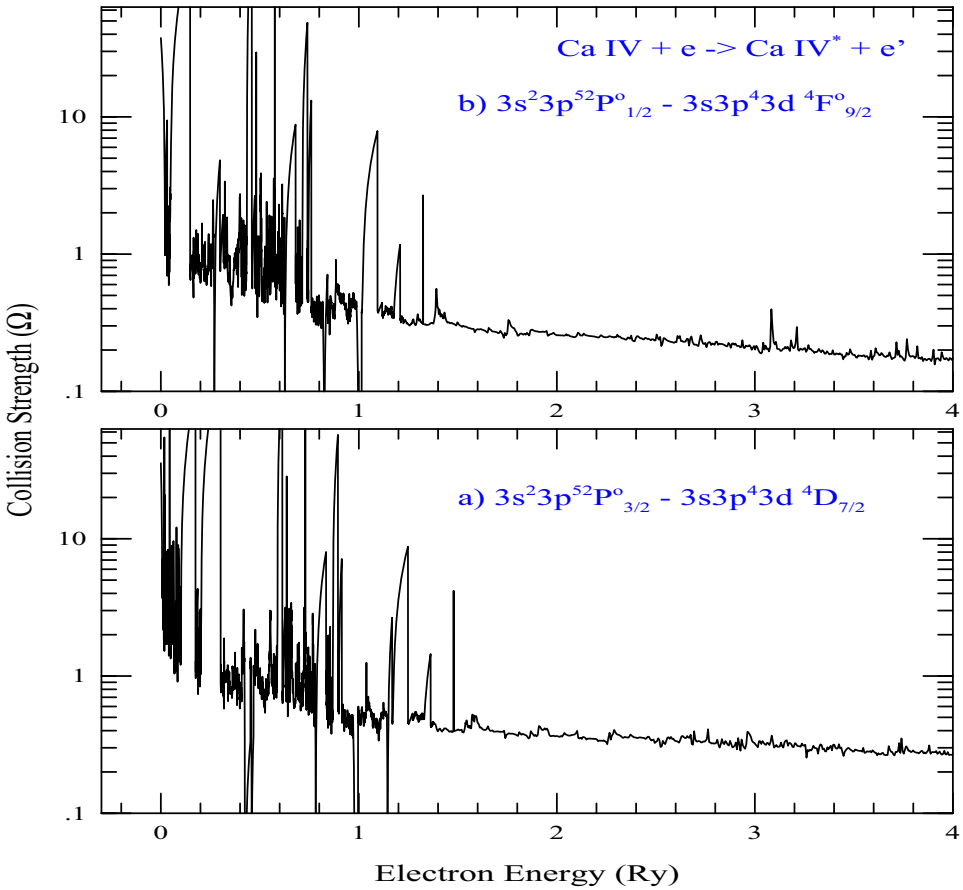

Fig. 3 Collision strength for forbidden excitation **a** $\Omega(3s^2 3p^5\ {}^2P^o_{3/2} - 3s^2 3p^4 4s\ {}^4D_{7/2})$ and **b** $\Omega(3s^2 3p^5\ {}^2P^o_{3/2} - 3s^2 3p^4 4s\ {}^4F_{9/2})$ in extreme ultraviolet, 496 Åand 458 Å, respectively, illustrating resonant features in the low-energy region and decreasing background in the high-energy region

energy levels are found to become weaker. Such weakening indicates convergence of resonant contributions to the collisional parameters.

The lower panel of Fig. 2 presents the effective collision strength (Υ) for $\Omega[({}^2P^o_{3/2} - {}^2P^o_{1/2})$. Starting low at lower energy, Υ forms a shoulder bump at 10^4 K. Then it rises relatively quickly, reaching the high peak value 9.66 at about 3×10^5 K. The peak indicates the presence of a strong line of the transition in Ca IV which can be detected. The intensity of the line will depend on the plasma environment.

We present illustrative examples of forbidden transitions in Ca IV. Figure 3 presents collision strengths for two forbidden excitations in Ca IV, (a) $\Omega(3s^2 3p^5\ {}^2P^o_{3/2} - 3s^2 3p^4 4s^4 D_{7/2})$ and (b) $\Omega(3s^2 3p^5\ {}^2P^o_{3/2} - 3s^2 3p^4 4s^4 F_{9/2})$. Both transitions show the presence of strong resonances in the lower-energy region. The resonances become weaker in the higher-energy region, indicating that the contribution of resonances is converging. This is the typical trend of Ω for forbidden transitions. Both of these transitions lie in the extreme ultraviolet region, with wavelengths of 496 and 458 Å, respectively.

Collision strengths for dipole-allowed transitions may show a different trend in the high-energy background from those of forbidden transitions. The dipole in the target can affect the partial waves of the incident electron and contribute to the collision strength. The contribution depends on the oscillator strength for the dipole transition. For stronger transitions, inclusion of a larger number of partial waves is important for converged contributions.

Figure 4 presents features of Ω (EIE) for two dipole-allowed transitions to low-lying excited levels, (a) $3\,s^2 3p^5\ {}^2P^o_{1/2} - 3s3p^6\ {}^2S_{1/2}$ (levels 2–3) at 670 Åand (b) $3s^2 3p^5\ {}^2P^o_{3/2} - 3p^4 3d\ {}^2D_{5/2}$ (levels 1–18) at 435 Å. Ω for these transitions show the presence of prominent resonances in the lower-energy regions, which become weaker converging to a smooth background at higher energy. It can be noted that the high-energy background is decreasing very slowly or remaining almost constant. These transitions are much weaker than others, as indicated by their smaller values for the oscillator strengths and A-values presented in Table 2.

Figure 5 presents Ω for dipole-allowed excitation of (a) $3s^2 3p^5\ {}^2P^o_{3/2} - (3s^2 3p^4 3d)^2 D_{5/2}$ at 340 Åand (b) $3s^2 3p^5\ {}^2P^o_{3/2} - (3s^2 3p^4 4s)\ {}^2P_{3/2}$ at 332 Åin Ca IV. The high peak resonances are converging near 1 Ry. Although there are many more core ion excita-

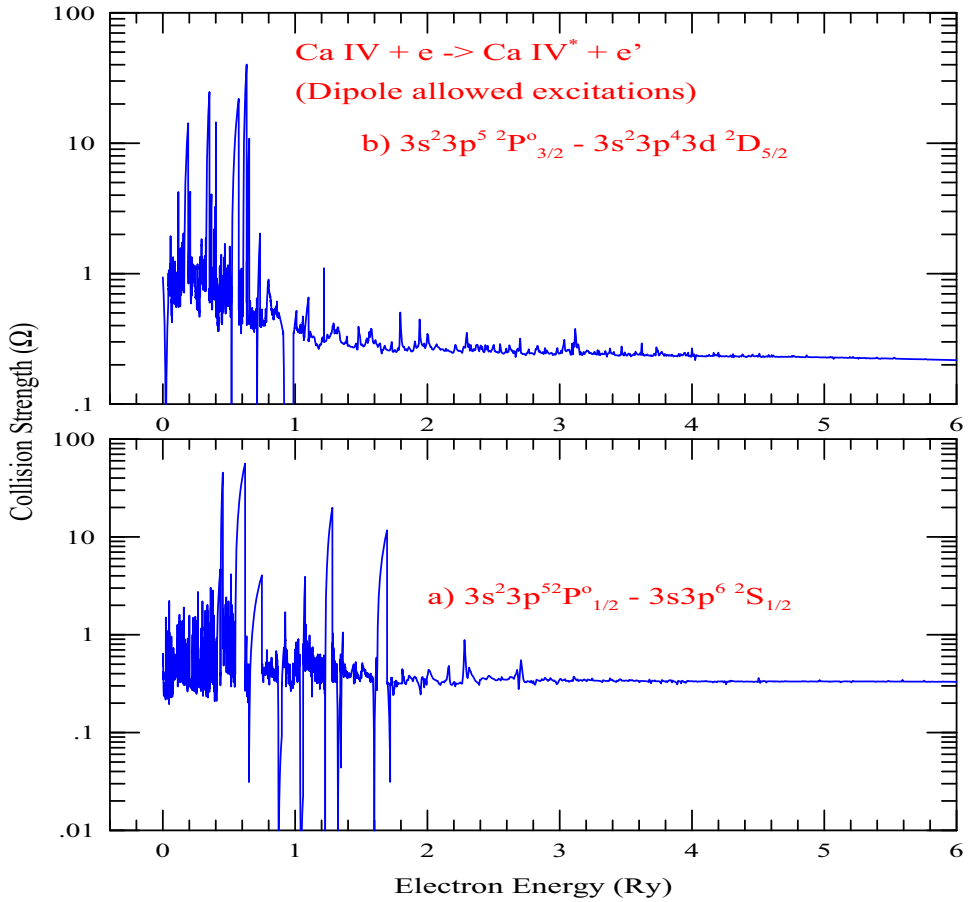

Fig. 4 Features of $\Omega(EIE)$ for two weaker dipole-allowed transitions (oscillator strengths are given in Table 2): **a** $3s^2 3p^5\ {}^2P^o_{1/2} - 3s3p^6\ {}^2S_{1/2}$ (levels 2–3) and **b** relatively higher transition $3\,s^2 3p^5\ {}^2P^o_{3/2} - 3\,s^2 3p^4 3d^2 D_{5/2}$ (levels 1–18). Resonances have converged to a smooth background at high energy where the background remains almost constant or decreases slowly with increase of energy, typical for weak transitions

Table 2 Dipole-allowed transitions between levels i and j, their f- and A-values, and transition wavelength λ_{ij} in angstroms for the illustrated examples of Ω of Ca IV in Figs. 4 and 5

Figure	i–j	$SL\pi J$		λ_{ij} (Å)	f_{ij}	$A_{ji}(\mathrm{s}^{-1})$
		i	j			
4a	2–3	${}^2P^o_{1/2}$	${}^2S_{1/2}$	670	1.55E−02	2.01E+08
4b	1–18	${}^2P^o_{3/2}$	${}^2D_{5/2}$	435	8.14E−03	1.98E+08
5a	1–33	${}^2P^o_{3/2}$	${}^2D_{5/2}$	319	2.60E+00	1.14E+11
5b	1–30	${}^2P^o_{3/2}$	${}^2P_{3/2}$	332	1.09E+00	7.10E+10

The level indices i and j correspond to those in Table 1

tions included in the wave function expansion, their Rydberg series of resonances have become weak, with almost no contributions to Ω. This indicates convergence in the wave function expansion for generating resonant features. However, the background of Ω is rising with energy toward a plateau. This trend is in agreement with the expected Coulomb–Bethe behavior of $\Omega_{if}(E) \sim_{E\to\infty} dln(E)$ (Eq. 10) at high energy for transitions with stronger or larger values for oscillator strength or A-values. The f- and A-values for the two transitions are given in Table 2. As discussed above, for these transitions, a larger number of partial waves must be considered in calculating Ω. There may not be a rising trend toward a plateau with an inadequate number of partial waves. In this case, Ω is often extrapolated with Coulomb–Bethe form.

Astrophysical models require temperature-dependent effective collision strength (ϒ). Table 3 presents ϒ for some excitations to levels that could be of importance for astrophysical applications. ϒ for any other excitation of the 1431 transitions can be computed by averaging Ω over the Maxwellian distribution function at

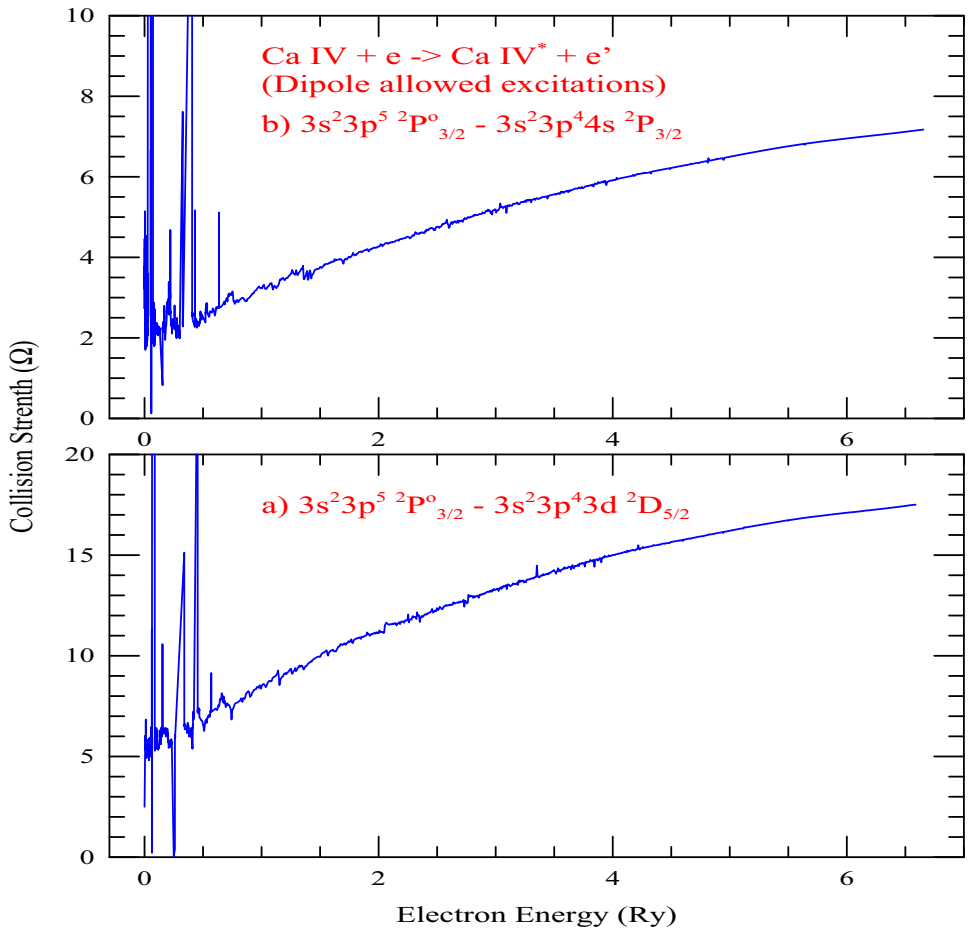

Fig. 5 Features of Ω for excitation to high-lying dipole-allowed levels, **a** $3s^2 3p^5\ {}^2P^o_{3/2} - (3s^2 3p^4 3d)^2 D_{5/2}$ and **b** $3s^2 3p^5\ {}^2P^o_{3/2} - (3s^2 3p^4 4s)\ {}^2P_{3/2}$, with stronger or larger values for oscillator strengths illustrating **a** convergence of resonances and **b** rising Coulomb–Bethe $ln(E)$ behavior of Ω at higher energy. The background of Ω rises toward forming a plateau

any temperature. The Ω values and ϒ for a number of excitations, in addition to those presented here, are available electronically at NORAD-Atomic-Data [28].

4.2 Energy levels and radiative transition parameters of Ca IV

We present about 93,000 radiative transition rates for Ca IV obtained from atomic structure calculations in Breit–Pauli approximation implemented in SUPERSTRUCTURE. The 13 configurations of Ca IV, listed in the Computation section, resulted in 387 fine-structure energy levels and 93,296 radiative transitions of types allowed (E1) and forbidden (E2, E3, M1, M2).

Our calculated energies for Ca IV have been compared with the measured values in Table 1 in the Computation section. They are in good agreement with the observed energies available in the NIST table. As seen in Table 1, the differences between calculated and measured energies are within 5% for most of the levels except for the highest-lying $^4D^o$ and $^4F^o$ states, where the differences are about 8%.

The A-values have been benchmarked with a limited number of available data. The present transition probabilities are compared in Table 4 with the only three available A-values in the NIST compilation and with those available from other sources. Transition $3s^2 3p^5(^2P^o_{3/2}) \rightarrow 3s^2 3p^5(^2P^o_{1/2})$ can be both M1 and E2 types. The present A-value for the M1 transition, 0.545, is in excellent agreement with 0.543 of Naqvi [12]. The present value is also in good agreement with 0.379 by Huang et al. [15], given the typical magnitude of A-values of the order of 10^8 s^{-1} or higher for E1 transitions. Similarly to the very weak E2 transition, the present A-value of $3.82 \times 10^{-}05\,s^{-1}$ is also in very good agreement with $1.906 \times 10^{-}05\,s^{-1}$ of Huang et al. [15]. For the first dipole-allowed transitions $3s^2 3p^5(^2P^o_{3/2,1/2}) \rightarrow 3s3p^6(^2S_{1/2})$, the present A-values agree very well with those of Wilson et al. [16] but differ from Huang et al. and Varsavsky [13], who also differ from each other and from Wilson et al. As

Table 3 ϒ at various temperatures for different excitations of levels 1–2 to 1–18 in Ca IV

logT	T (K)	ϒ: 1–2	1–3	2–3	1–4	1–5
2.00	1.000E+02	9.312E−01	1.038E+00	5.709E−01	3.274E+01	2.158E−01
2.10	1.265E+02	9.339E−01	1.061E+00	5.674E−01	3.199E+01	2.395E−01
2.20	1.600E+02	9.382E−01	1.075E+00	5.587E−01	3.104E+01	2.827E−01
2.31	2.024E+02	9.439E−01	1.077E+00	5.447E−01	2.986E+01	3.545E−01
2.41	2.560E+02	9.507E−01	1.065E+00	5.261E−01	2.841E+01	4.608E−01
2.51	3.237E+02	9.581E−01	1.040E+00	5.037E−01	2.669E+01	6.014E−01
2.61	4.095E+02	9.654E−01	1.002E+00	4.791E−01	2.474E+01	7.688E−01
2.71	5.179E+02	9.722E−01	9.568E−01	4.537E−01	2.261E+01	9.507E−01
2.82	6.551E+02	9.785E−01	9.081E−01	4.294E−01	2.042E+01	1.134E+00
2.92	8.286E+02	9.851E−01	8.608E−01	4.081E−01	1.826E+01	1.315E+00
3.02	1.048E+03	9.948E−01	8.192E−01	3.909E−01	1.623E+01	1.503E+00
3.12	1.326E+03	1.014E+00	7.854E−01	3.784E−01	1.440E+01	1.724E+00
3.22	1.677E+03	1.054E+00	7.604E−01	3.702E−01	1.284E+01	2.002E+00
3.33	2.121E+03	1.127E+00	7.436E−01	3.654E−01	1.156E+01	2.335E+00
3.43	2.683E+03	1.242E+00	7.345E−01	3.634E−01	1.055E+01	2.690E+00
3.53	3.393E+03	1.395E+00	7.321E−01	3.635E−01	9.865E+00	3.018E+00
3.63	4.292E+03	1.572E+00	7.354E−01	3.655E−01	9.610E+00	3.292E+00
3.73	5.429E+03	1.752E+00	7.433E−01	3.694E−01	9.976E+00	3.553E+00
3.84	6.866E+03	1.920E+00	7.551E−01	3.750E−01	1.113E+01	3.947E+00
3.94	8.685E+03	2.064E+00	7.705E−01	3.844E−01	1.312E+01	4.689E+00
4.04	1.099E+04	2.185E+00	7.909E−01	4.056E−01	1.577E+01	5.927E+00
4.14	1.389E+04	2.294E+00	8.220E−01	4.587E−01	1.869E+01	7.609E+00
4.24	1.758E+04	2.411E+00	8.747E−01	5.748E−01	2.139E+01	9.464E+00
4.35	2.223E+04	2.560E+00	9.640E−01	7.800E−01	2.341E+01	1.113E+01
4.45	2.812E+04	2.759E+00	1.101E+00	1.073E+00	2.448E+01	1.232E+01
4.55	3.556E+04	3.016E+00	1.285E+00	1.419E+00	2.455E+01	1.288E+01
4.65	4.498E+04	3.353E+00	1.497E+00	1.762E+00	2.373E+01	1.282E+01
4.76	5.690E+04	3.841E+00	1.708E+00	2.047E+00	2.222E+01	1.224E+01
4.86	7.197E+04	4.576E+00	1.886E+00	2.241E+00	2.024E+01	1.130E+01
4.96	9.103E+04	5.599E+00	2.007E+00	2.331E+00	1.803E+01	1.015E+01
5.06	1.151E+05	6.818E+00	2.060E+00	2.323E+00	1.574E+01	8.907E+00
5.16	1.456E+05	8.028E+00	2.045E+00	2.234E+00	1.353E+01	7.674E+00
5.27	1.842E+05	8.996E+00	1.975E+00	2.088E+00	1.147E+01	6.514E+00
5.37	2.330E+05	9.559E+00	1.865E+00	1.907E+00	9.610E+00	5.464E+00
5.47	2.947E+05	9.661E+00	1.733E+00	1.711E+00	7.982E+00	4.541E+00
5.57	3.728E+05	9.347E+00	1.592E+00	1.516E+00	6.583E+00	3.745E+00
5.67	4.715E+05	8.718E+00	1.453E+00	1.332E+00	5.398E+00	3.072E+00
5.78	5.964E+05	7.893E+00	1.324E+00	1.165E+00	4.408E+00	2.509E+00
5.88	7.543E+05	6.978E+00	1.207E+00	1.018E+00	3.589E+00	2.044E+00
5.98	9.541E+05	6.058E+00	1.105E+00	8.908E−01	2.917E+00	1.663E+00
6.08	1.207E+06	5.187E+00	1.017E+00	7.837E−01	2.370E+00	1.352E5+00
logT	T (K)	ϒ: 1–6	1–7	1–12	1–13	1–18
6.18	1.526E+06	4.398E+00	9.435E−01	6.943E−01	1.927E+00	1.101E+00
6.29	1.931E+06	3.705E+00	8.822E−01	6.205E−01	1.570E+00	8.981E−01
6.39	2.442E+06	3.112E+00	8.317E−01	5.602E−01	1.283E+00	7.353E−01
6.49	3.089E+06	2.612E+00	7.906E−01	5.113E−01	1.053E+00	6.050E−01
6.59	3.907E+06	2.198E+00	7.572E−01	4.718E−01	8.700E−01	5.010E−01
6.69	4.942E+06	1.857E+00	7.303E−01	4.400E−01	7.238E−01	4.181E−01
6.80	6.251E+06	1.579E+00	7.087E−01	4.146E−01	6.075E−01	3.521E−01
6.90	7.906E+06	1.354E+00	6.914E−01	3.942E−01	5.151E−01	2.997E−01
7.00	1.000E+07	1.173E+00	6.776E−01	3.780E−01	4.417E−01	2.580E−01

Table 3 continued

logT	T (K)	ϒ: 1–2	1–3	2–3	1–4	1–5
2.00	1.000E+02	1.307E+00	4.810E−01	4.444E−01	8.154E−01	9.113E−01
2.10	1.265E+02	1.221E+00	4.936E−01	4.540E−01	8.560E−01	9.043E−01
2.20	1.600E+02	1.164E+00	5.075E−01	4.647E−01	9.006E−01	8.956E−01
2.31	2.024E+02	1.136E+00	5.222E−01	4.758E−01	9.425E−01	8.845E−01
2.41	2.560E+02	1.131E+00	5.374E−01	4.866E−01	9.756E−01	8.705E−01
2.51	3.237E+02	1.147E+00	5.526E−01	4.963E−01	9.969E−01	8.528E−01
2.61	4.095E+02	1.175E+00	5.670E−01	5.042E−01	1.008E+00	8.304E−01
2.71	5.179E+02	1.210E+00	5.797E−01	5.102E−01	1.014E+00	8.023E−01
2.82	6.551E+02	1.246E+00	5.902E−01	5.195E−01	1.028E+00	7.675E−01
2.92	8.286E+02	1.285E+00	5.983E−01	5.546E−01	1.077E+00	7.260E−01
logT	T (K)	ϒ: 1–6	1–7	1–12	1–13	1–18
3.02	1.048E+03	1.335E+00	6.038E−01	6.781E−01	1.206E+00	6.795E−01
3.12	1.326E+03	1.414E+00	6.065E−01	1.021E+00	1.485E+00	6.321E−01
3.22	1.677E+03	1.533E+00	6.080E−01	1.804E+00	2.005E+00	5.891E−01
3.33	2.121E+03	1.690E+00	6.163E−01	3.326E+00	2.872E+00	5.558E−01
3.43	2.683E+03	1.873E+00	6.615E−01	5.914E+00	4.173E+00	5.359E−01
3.53	3.393E+03	2.079E+00	8.171E−01	9.770E+00	5.920E+00	5.317E−01
3.63	4.292E+03	2.336E+00	1.199E+00	1.478E+01	7.988E+00	5.465E−01
3.73	5.429E+03	2.688E+00	1.911E+00	2.039E+01	1.011E+01	5.866E−01
3.84	6.866E+03	3.169E+00	2.955E+00	2.576E+01	1.198E+01	6.590E−01
3.94	8.685E+03	3.769E+00	4.202E+00	3.003E+01	1.332E+01	7.674E−01
4.04	1.099E+04	4.427E+00	5.432E+00	3.264E+01	1.402E+01	9.097E−01
4.14	1.389E+04	5.047E+00	6.429E+00	3.343E+01	1.406E+01	1.080E+00
4.24	1.758E+04	5.531E+00	7.061E+00	3.259E+01	1.357E+01	1.273E+00
4.35	2.223E+04	5.813E+00	7.294E+00	3.053E+01	1.268E+01	1.480E+00
logT	T (K)	ϒ: 1–6	1–7	1–12	1–13	1–18
4.45	2.812E+04	5.870E+00	7.175E+00	2.768E+01	1.154E+01	1.685E+00
4.55	3.556E+04	5.718E+00	6.789E+00	2.446E+01	1.029E+01	1.865E+00
4.65	4.498E+04	5.401E+00	6.230E+00	2.117E+01	9.026E+00	1.993E+00
4.76	5.690E+04	4.969E+00	5.576E+00	1.802E+01	7.809E+00	2.053E+00
4.86	7.197E+04	4.469E+00	4.890E+00	1.514E+01	6.679E+00	2.038E+00
4.96	9.103E+04	3.942E+00	4.216E+00	1.258E+01	5.656E+00	1.956E+00
5.06	1.151E+05	3.420E+00	3.583E+00	1.036E+01	4.749E+00	1.825E+00
5.16	1.456E+05	2.926E+00	3.009E+00	8.470E+00	3.957E+00	1.663E+00
5.27	1.842E+05	2.474E+00	2.502E+00	6.885E+00	3.277E+00	1.487E+00
5.37	2.330E+05	2.072E+00	2.064E+00	5.571E+00	2.700E+00	1.312E+00
5.47	2.947E+05	1.722E+00	1.691E+00	4.490E+00	2.215E+00	1.145E+00
5.57	3.728E+05	1.423E+00	1.378E+00	3.608E+00	1.812E+00	9.941E−01
5.67	4.715E+05	1.170E+00	1.118E+00	2.892E+00	1.479E+00	8.604E−01
5.78	5.964E+05	9.593E−01	9.047E−01	2.314E+00	1.207E+00	7.448E−01
5.88	7.543E+05	7.849E−01	7.303E−01	1.849E+00	9.842E−01	6.467E−01
5.98	9.541E+05	6.418E−01	5.888E−01	1.477E+00	8.038E−01	5.646E−01
6.08	1.207E+06	5.252E−01	4.744E−01	1.179E+00	6.582E−01	4.965E−01
6.18	1.526E+06	4.307E−01	3.824E−01	9.408E−01	5.410E−01	4.407E−01
6.29	1.931E+06	3.544E−01	3.087E−01	7.513E−01	4.471E−01	3.953E−01
6.39	2.442E+06	2.931E−01	2.497E−01	6.007E−01	3.719E−01	3.585E−01
6.49	3.089E+06	2.440E−01	2.027E−01	4.809E−01	3.119E−01	3.288E−01
6.59	3.907E+06	2.047E−01	1.652E−01	3.859E−01	2.641E−01	3.050E−01
6.69	4.942E+06	1.734E−01	1.354E−01	3.106E−01	2.261E−01	2.859E−01
6.80	6.251E+06	1.485E−01	1.117E−01	2.508E−01	1.959E−01	2.707E−01
6.90	7.906E+06	1.287E−01	9.292E−02	2.035E−01	1.719E−01	2.586E−01
7.00	1.000E+07	1.129E−01	7.802E−02	1.661E−01	1.529E−01	2.490E−01

Table 4 Comparison of present A-values for Ca-IV with those available in the literature

K	KP	λ (Å)	Transition	A (Present) (s^{-1})	A (Others) (s^{-1})
1	2		$3s^23p^5(^2P^o_{3/2}) \rightarrow 3s^23p^5(^2P^o_{1/2})$	M1:0.545	M1:0.541 [12],0.3786 [15]
1	2		$3s^23p^5(^2P^o_{3/2}) \rightarrow 3s^23p^5(^2P^o_{1/2})$	E2:3.82e−5	E2:1.906E−5 [15]
1	3	656	$3s^23p^5(^2P^o_{3/2}) \rightarrow 3s3p^6(^2S_{1/2})$	5.11E+8 4.22E+8	7.425E+8 [16],1.20E+10 [13], 1.09e+10 [15]
2	3	669.7	$3s^23p^5(^2P^o_{1/2}) \rightarrow 3s3p^6(^2S_{1/2})$	2.466E+8 2.01E+8	3.529E+8 [16], 5.4E+9 [13]
1	10	454.6	$3s^23p^5(^2P^o_{3/2}) \rightarrow 3s^23p^43d(^4F_{5/2})$	1.84E+6	1.692E+6 [16]
1	12	543	$3s^23p^5(^2P^o_{3/2}) \rightarrow 3s^23p^43d(^2P_{1/2})$	9.696E+6 9.57E+6	7.889E+6 [16]
2	12	459.5	$3s^23p^5(^2P^o_{1/2}) \rightarrow 3s^23p^43d(^2P_{1/2})$	3.930E+7 3.87E+7	3.503E+7 [16]
1	14	440	$3s^23p^5(^2P^o_{3/2}) \rightarrow 3s^23p^43d(^4P_{1/2})$	1.350E+7 1.31E+7	1.243E+7 [16]
1	15	439	$3s^23p^5(^2P^o_{3/2}) \rightarrow 3s^23p^43d(^4P_{3/2})$	3.90E+6 3.77E+6	5.367E+6 [16]
1	16	437.3	$3s^23p^5(^2P^o_{3/2}) \rightarrow 3s^23p^43d(^4P_{5/2})$	2.740E+6 2.66E+6	2.754E+6 [16]
1	17	437.8	$3s^23p^5(^2P^o_{3/2}) \rightarrow 3s^23p^43d(^2D_{3/2})$	6.530E+7 6.45E+7	5.201E+7 [16]
1	18	434.6	$3s^23p^5(^2P^o_{3/2}) \rightarrow 3s^23p^43d(^2D_{5/2})$	1.920E+8 1.90E+8	1.576E+8 [16]
1	27	341.3	$3s^23p^5(^2P^o_{3/2}) \rightarrow 3s^23p^43d(^2S_{1/2})$	6.23E+10 6.43E+10	4.264E+10 [16], 6.543E+10 [15]

For the E1 transitions, the first A-value from the present work represents the use of experimental transition energy, and the second one (below it) of calculated energy. K and KP are the initial and final transitional energy level indices (as given in Table 1), and λ is the transition wavelength in angstroms. The references are given in superscripts

Table 5 Lifetimes of a few levels illustrating the complete table of lifetimes of all 386 levels

Type	LSi	Ci	gi	lvi	LSj	Ci	gj	lvj	f(E1)/S(E2,E3,M1,M2)	Aji (s^{-1})	Eij (AA)
lifetime: sslevel j= 2, Cf= 1, $^2P^o_{1/2}$ [E= 3.019E−02 Ry= 3.3134852E+03 /cm]											
E2	$^2P^o$	1	4	1	$^2P^o$	1	2	2	1.54E+00	5.180E−05	3.0180E+04
M1	$^2P^o$	1	4	1	$^2P^o$	1	2	2	1.33E+00	6.540E−01	3.0180E+04
Summed A-values: Af (forbidden) = 6.541E−01, Aa(allowed) = 0.000E+00 s-1											
Total sum(Af+Aa) = Aji (2 transitions) to the level= 6.541E−01 s-1											
Lifetime (= 1/Aji) = 1.529E+00 s											
lifetime: sslevel j = 7, cf = 3, $^4D_{1/2}$ [E = 1.826E+00 Ry = 2.0041544E+05/cm]											
E1i	$^2P^o$	1	4	1	^4D	3	2	7	1.01E−06	5.420E+04	4.9896E+02
E1i	$^2P^o$	1	2	2	^4D	3	2	7	3.96E−06	1.030E+05	5.0735E+02
E2	^2S	2	2	3	^4D	3	2	7	0.00E+00	0.000E+00	1.7417E+03
M1	^2S	2	2	3	^4D	3	2	7	3.18E−07	8.120E−04	1.7417E+03
E2	^4D	3	6	5	^4D	3	2	7	1.15E−03	2.890E−12	2.0196E+05
E2	^4D	3	6	5	^4D	3	2	7	1.15E−03	2.890E−12	2.0196E+05
E2	^4D	3	4	6	^4D	3	2	7	2.69E−03	1.120E−13	4.5789E+05
M1	^4D	3	4	6	^4D	3	2	7	5.97E+00	8.380E−04	4.5789E+05
Summed A-values: Af (forbidden) = 1.650E−03, Aa (allowed) = 1.572E+05 s-1											
Total sum(Af+Aa)= Aji(8 transitions) to the level = 1.572E+05 s-1											
Lifetime (= 1/Aji) = 6.361E−06 s											

Radiative decay rates of level j to various lower levels $j \rightarrow i$ are given. Notation C is for configuration, g for statistical weight factor, lv for level, f for f-value for an E1 transition or S-values for E2, E3, M1, M2 transitions, A for A-value and E for transition energy

Table 4 shows, the present results are in agreement with those of Wilson et al. for other transitions.

We provide two calculated A-values for the dipole-allowed transitions in order to compare the accuracy. The first A-value has been obtained using the experimental transition energy, and the second one, below it, using the calculated energy. We can see that they do not differ significantly from each other. Some differences among the results are expected due to the use of different optimizations of the configurations included in each calculation and the accuracy in the methods considered for calculations of the transition parameters.

The present work provides lifetimes of all 386 excited levels in a file that is available electronically at NORAD-Atomic-Data [28]. The lifetime of an excited level can be calculated if the A-values or the radiative decay rates of the level to the lower levels are known. Lifetimes are measurable at experimental setups. Table 5 presents lifetimes of a few levels to illustrate their values. For each excited level in the table, the level number, configuration number, spectroscopic notation and energy are given. This line is followed by the A-values of the level decaying to lower levels. The A-values are added and the sum is inverted to obtain the lifetime. Levels decaying through the forbidden transitions (E2,E3,M1,M2) have longer lifetimes than those through dipole-allowed transitions (same spin E1d and intercombination E1i). No lifetimes for Ca-IV levels were found in the literature for comparison. However, their accuracies are related to those of the A-values which have been discussed for Table 4.

5 Conclusion

We have studied the collision strength of Ca IV using a 54-level close-coupling wave function expansion that corresponds to target ion excitations to high-lying levels. This ensures inclusion of converged contributions of resonances generated by all the levels. We have demonstrated the effect of the number of partial waves in the collision strength Ω and showed convergence of partial waves contributing to collision strengths.

Features of Ω show resonances in the low-energy region but they converge to the background long before reaching the highest (54th) excitation of Ca IV. We find that Ω of the emission line of 3.2 μm due to collisional excitation of $^2P^o_{3/2} - ^2P^o_{1/2}$ of ground configuration $3s^2 3p^5$ has extensive resonances with enhanced background in the low-energy region. This has resulted in a strong effective collision strength Υ with a peak around 3×10^5 K indicating the distinct presence of an emission line when the environmental plasma effects are low. The 3.2 μm line is within the wavelength range of the JWST.

The present Ω shows expected features at high electron energy, such as decaying background for the forbidden transitions, slow decay or almost constant values for weak dipole transitions and rising trend of Coulomb–Bethe $\ln(E)$ behavior toward a plateau for strong dipole-allowed transitions.

We present a set of over 93,000 radiative transitions among 387 energy levels with orbitals up to 5 s in Ca IV. Results include the lifetimes of all 386 excited levels.

The present results are expected to be accurate and large enough for the two processes to provide a complete astrophysical modeling for all practical purposes.

Acknowledgements All computations were carried on the high-performance computers of the Ohio Supercomputer Center. BS acknowledges the IRSIP fellowship from the Government of Pakistan to carry out the research at the Ohio State University.

Author contributions

Both authors, S.N. Nahar and B. Shafique, contributed equally to the contents of the paper. While SNN trained BS, set up the project, wrote necessary program, and remained engaged in studying the project, BS picked up all aspects of computations, carried out computations, and was engaged in the analysis.

Data Availability Statement This manuscript has associated data in a data repository. [Authors' comment: All atomic data for energies, radiative transitions, collisional excitations, and effective collision strengths of a set of transitions are available online at the NORAD-Atomic-Data database at the Ohio State University at: https://norad.astronomy.osu.edu/.]

References

1. S.N. Shore, T. Augusteijn, A. Ederoclite, H. Uthas, A&A **533**, L8 (2011)
2. M. Asplund, N. Grevesse, A.J. Sauval, P. Scott, Annu. Rev. Astron. Astrophys. **47**, 481–52 (2009)
3. J. Shepherd (2019) https://www.astrobin.com/full/406485/0/
4. W.V. Jacobson-Galan et al., Astrophys. J. **898**, 166 (2020)
5. H. Feuchtgruber et al., ApJ **487**, 962 (1997)
6. R. Ignanc, J.P. Cassinelli, M. Quigley, B. Babler, ApJ **558**, 771–779 (2001)
7. H. Feuchtgruber, D. Lutz, D.A. Beintema, ApJS **136**, 221 (2001)
8. B. Zuckerman, D. Koester, I.N. Reid, M. Hunsch, ApJ **596**, 477 (2003)
9. A.K. Pradhan, S.N. Nahar, *Atomic Astrophysics and Spectroscopy* (Cambridge University Press, New York, 2011)
10. J. Sugar, C. Corliss, J. Phys. Chem. Ref. Data **14**(Suppl. 2), 1–664 (1985)
11. https://physics.nist.gov/PhysRefData/ASD/levels_form.html
12. A.M. Naqvi, *PhD Thesis Harvard University* (1951) (data available at NIST)

13. C.M. Varsavsky, Astrophys. J. Suppl. Ser. **6**, 75–107 (1961)
14. B.C. Fawcett, A.H. Gabriel, Proc. Phys. Soc. **88**, 262 (1966)
15. K.-N. Huang, Y.-K. Kim, K.T. Cheng, J.P. Desclaux, ADNDT**28**, 355–377 (1983)
16. N.J. Wilson, A. Hibbert, K.L. Bell, Phys. Scr. **61**, 603–610 (2000)
17. A.H. Gabriel, B.C. Fawcett, C. Jordan, Proc. Phys. Soc. **87**, 825 (1966)
18. D.G. Hummer, K.A. Berrington, W. Eissner, A.K. Pradhan, H.E. Saraph, J.A. Tully, Astron. Astrophys. **279**, 298–309 (1993)
19. K.A. Berrington, W. Eissner, P.H. Norrington, Comput. Phys. Commun. **92**, 290–420 (1995)
20. W. Eissner, M. Jones, H. Nussbaumer, Comput. Phys. Commun. **8**, 270–306 (1974)
21. S.N. Nahar, W. Eissner, G.X. Chen, A.K. Pradhan, A&A **408**, 789 (2003)
22. P.G. Burke, W.D. Robb, Adv. At. Mol. Phys. **11**, 143–214 (1975)
23. N.S. Scott, P.G. Burke, J. Phys. B **12**, 4299 (1980)
24. N.S. Scott, K.T. Taylor, Comput. Phys. Commun. **25**, 347 (1982)
25. A. Burgess, J.A. Tully, J. Phys. B **11**, 4271 (1978)
26. S.N. Nahar, Written in, unpublished (2013)
27. S.N. Nahar, Astron. Astrophys. Suppl. Ser. **127**, 253 (2000)
28. NORAD-Atomic-Data, https://norad.astronomy.osu.edu/